ACS OMEGA

Open Access



http://pubs.acs.org/journal/acsodf

Article

# Fabrication of Au Nanostructured Thin Film via Femtosecond Laser Glass Texturing for Enhanced Glucose Sensing

Filippo Franceschini,* Balasubramanian Nagarajan, Iliana Claes, Olivier Deschaume, Carmen Bartic, Sylvie Castagne, and Irene Taurino

Cite This: *ACS Omega* 2025, 10, 9165−9176

Read Online

ACCESS | Metrics & More | Article Recommendations | Supporting Information

**ABSTRACT:** Accurate glucose sensing is crucial for diabetes management, with nonenzymatic electrochemical devices promising enhanced durability and sensitivity. Nonetheless, widespread commercialization remains challenging, with the market still being dominated by their enzymatic counterparts. This study reports on the feasibility of femtosecond-laser texturing of glass followed by thin gold layer deposition to create a highly active and microchip-compatible glucose sensing platform. The laser treatment enables significant nanostructuring of the glass substrate, remarkably resulting in an 8 times greater surface area compared to flat gold films on glass. The electrodes were calibrated via both potentiostatic and potentiodynamic techniques. The laser-treated electrodes displayed in chronoamperometry a sensitivity to glucose of 63.9 ± 1.2 $\mu A \cdot cm^{-2} \cdot mM^{-1}$ in the 0.25 mM to 4 mM range and of 42.6 ± 0.8 $\mu A \cdot cm^{-2} \cdot mM^{-1}$ ranging from 5 mM to 10 mM. Compared to the flat film gold electrodes, the sensitivity was strikingly 5-fold and 10-fold greater for the two linear ranges. The effect of chlorides on gold was discussed both in terms of leaching from the Ag|AgCl reference electrode during sulfuric acid cycling and in terms of sensitivity decay in phosphate buffer solutions with physiological chloride concentrations. The combination of femtosecond-laser texturing with thin film deposition aims to facilitate the integration with preexisting glass-supported integrated sensing platforms, such as microfluidic systems for point-of-care applications. Its implementation offers substantial versatility, allowing for fine-tuning of the physicochemical properties of the electrode through straightforward adjustments in the deposition protocol parameters.

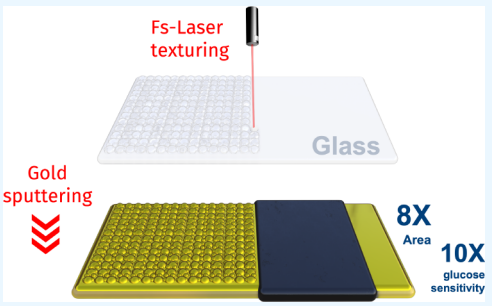


## INTRODUCTION

Diabetes is a critical worldwide health emergency, marked by an ever-increasing prevalence.[1] The effective management of this condition hinges on the precise measurement of blood glucose levels. In 1962, the pioneering work of Clark introduced the first electrochemical glucose sensor.[2] The device operated by entrapping the enzyme glucose oxidase in a semipermeable dialysis membrane over an oxygen electrode. Subsequent advancements significantly improved the performance of the enzymatic biosensors, first by the incorporation of artificial electron acceptors to improve the selectivity and reduce the oxygen-induced fluctuations[3] and later by enabling the direct electron transfer between the enzyme and the electrode through the utilization of conductive polymers and nanomaterials.[4] Although enzymatic glucose biosensors dominate the market, they are still riddled with significant limitations. Foremost among these are their sensitivity to temperature and pH, which complicates the sensor storage, transportation, and usage, ultimately necessitating replacement every 2 weeks.[5−8] In contrast, nonenzymatic sensors exhibit enhanced durability, superior sensitivity, and greater ease of miniaturization, as they are not constrained by the presence of macro-sized biomolecules.[9,10] Materials such as silver[11] or metal oxides (e.g., CuO,[12] $Co_3O_4$,[13] Ni,[14,15] and VOx[16]) are being investigated as nonenzymatic glucose electrocatalysts due to their low cost and high sensitivity. However, their activity is currently restricted to alkaline conditions, rendering them unsuitable for real-time monitoring applications. In contrast, noble metals (e.g., Pt,[17,18] Au,[19−21] Pd,[22−24] and Ir[25]) are promising candidates due to their unique capacity to oxidize glucose at a physiological pH of 7.4. Among these, Au has garnered significant interest over time due to its remarkable electroactivity for glucose oxidation,[26] despite its weak chemisorptive properties stemming from filled d-orbitals.[27] Due to their distinctive electronic configuration, gold electrodes are not susceptible to the blocking of active sites by the adsorption of glucose oxidation products, as opposed to other noble metals, such as Pt.[28] Furthermore, as far back as 1985, Vassilyev et al.[26] documented the superior glucose selectivity of Au in comparison to both Pt and Pt−Au alloys. Although gold electrodes lack a selective oxidation

Received: October 10, 2024
Revised: January 29, 2025
Accepted: January 31, 2025
Published: February 28, 2025

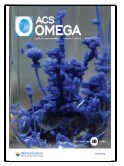

mechanism, the effect of interferents (e.g., ascorbic acid, uric acid, and acetaminophen) can be minimized by adjusting the amperometric potential.[29−31] This is also facilitated by the 20 to 40 times lower concentration of interferents in real body fluids compared to glucose.[32] Nonetheless, it should be noted that when used in vivo, amino acids can lead to surface fouling; thus, a semipermeable membrane, such as Nafion, should also be included in a ready-to-market design.[33,34] Critically, two important requirements also need to be addressed: resistance to chlorides and high sensitivity. Halide poisoning of Au is an insidious issue that leads to the deactivation of the catalyst at physiological chloride concentrations.[35,36] In light of this, it is essential to evaluate the performance of gold electrodes as a function of chloride concentration under real operating conditions. This assessment serves as a fundamental step toward the development of more poisoning-resilient electrodes. Conversely, sensitivity enhancements can be obtained more readily by increasing the surface area, and nanotechnology shows great promise in this regard. Various methods have been employed to fabricate nanostructured gold electrodes,[37,38] encompassing direct electrostatic assembly,[39] covalent linking,[40] polymer entrapment or comixing, sol−gel processes,[41] electrochemical etching,[42] and electrodeposition.[43] Nevertheless, many of these fabrication approaches entail the use of hazardous chemicals or involve cumbersome procedures, de facto limiting their large-scale manufacturability.

Recently, femtosecond-laser direct writing has emerged as a promising technique for the control of surface patterns, enabling precise manipulation over the physical and chemical properties of the interface.[44−47] Through the localized ablation of solid surfaces, it allows for the production of intricate micro/nanostructures with enhanced surface area[48−51] and superhydrophilic properties.[52−54] While it has been effectively employed in diverse fields such as micromachining,[55] photonic devices,[56] and microfluidics,[57,58] its application in the context of electrochemical sensors is still in the early stages. Previous investigations into femtosecond-laser treatments for glucose sensing include the work by Wang et al.[49] on copper foil electrodes and Gao et al.[59] on nickel foam electrodes. Later, Chen et al.[60] applied a similar approach to copper foam electrodes. Unfortunately, these bulk electrode treatments are hard to apply to microfabricated devices due to the inherent susceptibility of thin films to complete ablation.

Herein, we propose a process of femtosecond-laser glass nanostructuration, followed by thin layer deposition of Au. As a fabrication strategy, it aligns well with a cleanroom process flow while minimizing the catalyst loading and allowing for a wide range of adjustments in the deposition phase. This approach aims to streamline the integration with established glass-supported sensing platforms such as microfluidic systems for point-of-care applications. In parallel, it establishes a clear trajectory for advancing the field of integrated glucose sensors and other sensing technologies at large.

## EXPERIMENTAL SECTION

**Chemicals.** Potassium hydroxide (KOH, 86.2%) was purchased from VWR Chemicals (USA). Sodium phosphate monobasic ($NaH_2PO_4$, ≥98.0%), sodium phosphate dibasic heptahydrate ($Na_2HPO_4{\cdot}7\ H_2O$, ≥98.0%), D-glucose ($C_6H_{12}O_6$, ≥99.5%), potassium chloride (KCl, ≥99.0%), sulfuric acid ($H_2SO_4$, ≥95.0%), and nitric acid ($HNO_3$, 70%) were obtained from Sigma-Aldrich (Germany). All chemicals were used as received without further purification. Aqueous solutions were prepared using ultrapure water with a resistivity higher than 18 MΩ·cm.

**Sample Preparation.** Thin film gold electrodes were fabricated by using an RF magnetron sputtering technique with a deposition power of 50 W onto borosilicate glass wafers (Borofloat 33). The working pressure was $3.2 \times 10^{-3}$ mbar, and the base pressure was $5.5 \times 10^{-3}$ mbar. A photoresist (S1818) was applied to the surface at a rotation speed of 3000 rpm for 45″. Subsequently, the wafer was baked on a hot plate for 2 min at 100°C. After dicing into 7 × 14 mm, the photoresist was stripped by immersion in acetone for 5 min, followed by rinsing with acetone, isopropyl alcohol (IPA), and deionized water. Tape was applied to the produced electrodes, defining a geometrical surface area of 0.49 $cm^2$.

**Electrochemical Experiments.** Electrochemical experiments were conducted using a multichannel potentiostat (MultiPalmSens4, PalmSens, Netherlands) in a three-electrode configuration. The potentials were measured and referred to a triple junction AglAgCl reference electrode (Sigma-Aldrich, Germany). A platinum coil served as a counter electrode. For experiments conducted in $H_2SO_4$ solution, a triple junction RE with its outer bridge filled with 0.5 M $H_2SO_4$ solution was employed. For experiments conducted in PBS, a triple junction RE with its outer bridge filled with 0.1 M PBS was employed.

**Laser Texturing.** The fabrication of nanostructured gold electrodes was performed in two stages, starting with the laser treatment of a borosilicate glass wafer followed by the sputter deposition of a thin layer of gold. To texture the glass, a Yb:KGW femtosecond laser (CARBIDE, Light Conversion) with a maximum average power of 20 W, a pulse duration of 250 fs, and a wavelength of 1030 nm was used. The substrates were placed on a high-precision five-axis mechanical platform synchronized with a 2D galvo scanner. The laser beam had a Gaussian intensity profile with a spot size ($d_{(1/e)^2}$) of 16 μm. The borosilicate glass substrate was subjected to laser ablation using a laser energy of 2 μJ and a pulse repetition rate of 1 MHz. Two scanning passes were performed with a scanning speed of 1000 mm/s and a hatch spacing of 10 μm. The selection of parameters was determined through our own methodology.

**Surface Characterization.** The structured electrodes were characterized using a scanning electron microscope (Philips XL30 FEG) operating at an accelerating voltage of 10 keV. Grazing incidence X-ray diffraction (GIXRD) analysis was performed with a PANalytical X'Pert Pro diffractometer with a Cu Kα source. All GIXRD patterns were acquired without a monochromator and with an incident angle of 2°. For the AFM characterization, an Agilent 5500 AFM equipped with a MAC III controller was employed for morphological imaging in intermittent contact mode under ambient air conditions. MSNL-F probes (resonance frequency $f$ = 120 kHz, spring constant $k$ = 0.6 N/m, and tip radius of curvature < 12 nm) were utilized. The AFM topography images were processed using Gwyddion.[61] The images were leveled and line-corrected in Gwyddion, which was also used to calculate the RMS roughness (Sq). For both the bare and nanostructured electrodes, at least two areas were imaged and analyzed on three separately prepared samples.


https://doi.org/10.1021/acsomega.4c09270
ACS Omega 2025, 10, 9165−9176

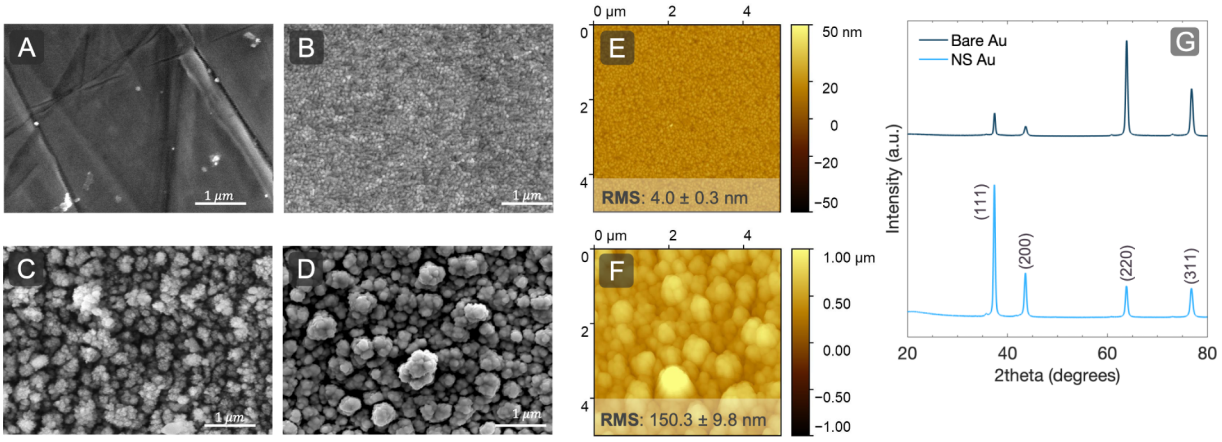


**Figure 1.** Secondary electron images at 20kX magnification of bare borosilicate glass (a), bare glass +300 nm of Au (Bare Au) (b), laser-structured borosilicate glass (c), and the borosilicate glass substrate covered with a 200 nm layer of Au (NS Au) (d); (e) atomic force microscopy image of Bare Au; (f) atomic force microscopy image of NS Au; (g) GI-XRD at a grazing angle of 0.5° of Bare Au and NS Au.

## RESULTS AND DISCUSSION

**Morphological and Crystallographic Characterization.** The surface morphology of the substrate as a result of femtosecond-laser texturing and the subsequent thin Au layer deposition was investigated using a scanning electron microscope (SEM). The untreated borosilicate glass wafer is shown in Figure 1a, displaying a surface devoid of submicrometer features, generally smooth with some scratch marks. Given the insulating nature of the glass substrate, 5 nm of Pd was deposited on top prior to imaging to avoid charging effects. Figure 1b shows the untreated glass substrate covered by a thin layer of Au (300 nm). We will henceforth refer to it as *"Bare Au"*. Clearly, the RF sputtered film follows the underlying substrate morphology well, resulting in a flat and even smoother surface. In contrast, the borosilicate glass wafer after irradiation with a femtosecond laser presents an extremely rough surface (Figure 1c), with hierarchical structures that range from tens of nanometers to at most a micron.

Material removal during fs laser texturing is a nonthermal process that occurs through mechanisms such as spallation, phase explosion, fragmentation, vaporization, and Coulomb explosion.[62,63] The observed surface morphology in this study (Figure 1c) can be attributed to the redeposition and fusion of nanoparticles resulting from vaporization,[64] which happens when the absorbed laser energy exceeds the cohesive energy of the irradiated material at higher laser fluences. On top of the roughened glass substrate, a thin film of Au (200 nm) was later deposited (Figure 1d). The selected thickness was the result of a compromise between conformality and complete coverage. This approach resulted in a fully covered Au surface, which well replicated nanofeatures of the underlying support. We will thus refer to this electrode as *"NS Au"*, standing for nanostructured Au. The impact of the difference in thickness between Bare Au and NS Au is negligible, as the glucose electrooxidation reaction is a surface process and the sheet resistance is known to be extremely similar for 200 and 300 nm sputtered Au films on glass.[65] Atomic force microscopy (AFM) measurements on three independent samples of Bare Au (Figure 1e) and NS Au (Figure 1f) reveal an almost 40-fold increase in root-mean-square roughness, from 4 to 150 nm. Grazing incidence X-ray diffraction analysis performed on Bare Au and NS Au samples (Figure 1e) revealed the presence of 4 diffraction peaks associated with Au for both electrodes, specifically, at 38.3°, 44.4°, 64.7°, and 76.6°, respectively, associated with the (111), (200), (220), and (311) crystal planes of face-centered cubic Au (JCPDS no. 04−0784). However, Bare Au exhibited different intensity ratios than expected, with the most intense peaks being associated with the (220) and (311) planes, as opposed to the (111) and (200) planes.[66,67] The prevalence of (220) crystallites over (111) crystallites has been documented by Chen et al.[68] in their investigation of Au thin films by e-beam evaporation on borosilicate glass. According to their findings, the high (200)/(111) intensity ratio was attributed to the differential growth rate of the crystallites in a the narrow thickness range of 100 nm−200 nm. The use of a different deposition technique and the presence of a Ti adhesion layer may explain why we observe a high (200)/(111) ratio for Bare Au at slightly greater thicknesses. In contrast, for NS Au, the intensity ratios matched very well with those in the literature, likely due to the highly textured nature of the support that mitigated any preferential growth. The average crystallite size was estimated with the Scherrer formula:

$$d = \frac{0.9\lambda}{\beta \cdot \cos\theta} \tag{1}$$

where "$\lambda$" is the wavelength of X-ray (0.1541 nm), "$\beta$" is the FWHM (full width at half-maximum), "$\theta$" is the diffraction angle, and "$d$" is the mean crystallite diameter. The calculated $d_{(111)}$ is marginally higher for Bare Au compared to NS Au, with the former exhibiting a mean size of 21.5 nm and the latter measuring 20.5 nm. Similarly, the value for $d_{(220)}$ is slightly greater in Bare Au, measuring 19.8 nm, in contrast to 17.4 nm in NS Au.

**Electroactive Area Determination and $H_2SO_4$ Cycling.** Having observed via SEM substantial morphological differences between the Bare Au and NS Au electrodes, it was necessary to determine in a quantitative way the increase in the surface area (SA) associated with the laser-treated samples. To do so, we implemented a procedure widely used in the literature[19,21,69] that consists of cycling the potential between −0.2 V and 1.6 V (vs AglAgCl) in an aqueous solution of 0.5 M $H_2SO_4$. Under these conditions, Au undergoes a process of surface oxide formation at anodic potentials (starting at ≈1 V vs AglAgCl), which gets subsequently reduced in the return


https://doi.org/10.1021/acsomega.4c09270
ACS Omega 2025, 10, 9165−9176

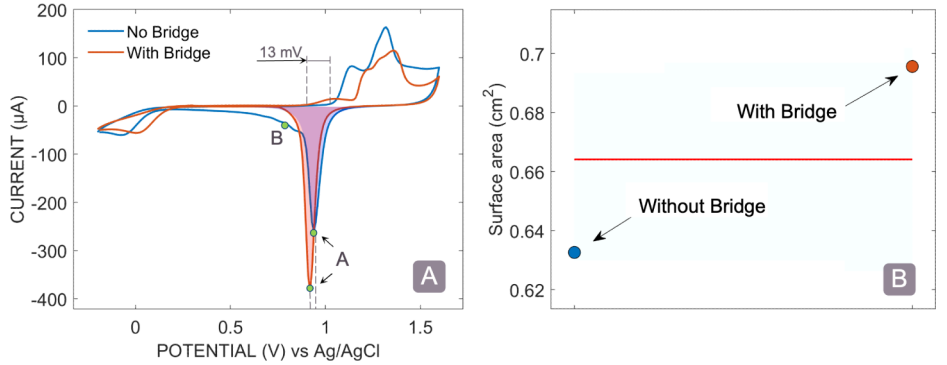


**Figure 2.** (a) Cyclic voltammograms in 0.5 M $H_2SO_4$ electrolyte solution for the Bare Au electrode with and without the use of a 0.5 M $H_2SO_4$ bridge; $\nu$ = 100 mV/s. (b) Calculated surface area by integration of the Au oxide reduction peak for the Bare Au electrode, with and without bridge.

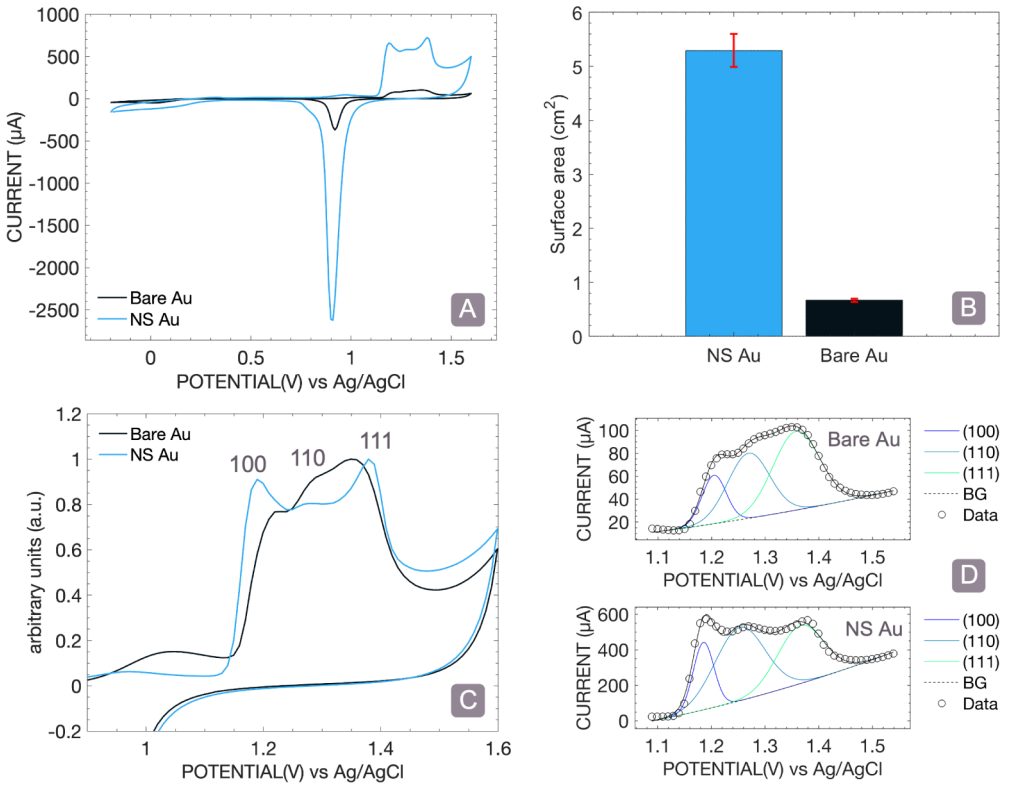


**Figure 3.** (a) Cyclic voltammograms in 0.5M $H_2SO_4$ electrolyte solution for the Bare Au and NS Au electrodes. (b) Calculated surface area by integration of the Au oxide reduction peak. (c) Cyclic voltammograms normalized with respect to the current maximum of Bare Au and NS Au in 0.5M $H_2SO_4$ (20th scan). (d) Cyclic voltammograms at the 20th cycle fitted in the region of oxide formation in 0.5M $H_2SO_4$ for the Bare Au and NS Au electrodes $\nu$ = 100 mV/s.

scan in a well-defined peak (peak A in Figure 2a). Under the approximation of a surface oxidation involving exactly a monolayer, the charge associated with its reduction is proportional to the SA of Au through eq 2.

$$SA = \frac{Q_0}{\nu \cdot Q_{os}} \tag{2}$$

where $Q_0$ corresponds to the area under the cathodic peak; $\nu$ represents the scan rate, and $Q_{os}$ = 384 C/cm$^2$ is the charge density required to reduce a monolayer of oxide per unit of the surface area.[70] An additional advantage of this procedure is the removal of contaminants from the surface, being successfully used as a relatively mild cleaning step.[71−73]

*The Effect of Chlorides on the Gold Oxide Formation and Reduction.* Although AgIAgCl reference electrodes are widely used both in analytical laboratories and in commercial glucose biosensors,[74] the instability of Au in the presence of mere traces of chlorides[35,75] complicates its practical use for the present application. To assess this issue, we monitored the cycle-to-cycle evolution of a Bare Au electrode in 0.5 M $H_2SO_4$ using a common double junction AgIAgCl reference electrode (Figure S1). Indeed, the chloride ions from the reference were observed to leak into the electrolyte and lead to the direct electrochemical dissolution of Au, in accordance with the findings of Xu et al.[76] The dissolution process involves the formation of soluble gold chloride complexes, following commonly proposed reactions:[77]



https://doi.org/10.1021/acsomega.4c09270
ACS Omega 2025, 10, 9165−9176

$$Au + 2Cl^- \rightarrow AuCl_2^- + e^- \quad E_0 = 1.15\ V \tag{3}$$

$$Au + 4Cl^- \rightarrow AuCl_4^- + 3e^- \quad E_0 = 1.00\ V \tag{4}$$

with reaction 33 reported[78,79] to dominate at more cathodic potentials (≈<1.1 V vs SCE) and lower $Cl^-$ concentration (<100 $\mu$M ), and reaction 44 at higher concentrations.[75,80] As a result, under these conditions, we expect mostly Au(III) complexes to form.

Consistent with the report of Tian et al.,[75] two anodic peaks at 1.1 and 1.3 V are observed (blue curve in Figure 2) that can be attributed to the combined effect of gold dissolution and oxide formation. In the return scan, the gold complexes resulting from the electrochemical dissolution can be reduced and redeposit gold on the surface. This leads to the emergence of a second cathodic peak at 0.8 V, labeled "peak B" in Figure 2a, in addition to the gold oxide reduction (peak A in Figure 2a). To minimize the effect of chloride leakage, a triple junction Ag|AgCl reference was employed with the outer bridge filled with 0.5 M $H_2SO_4$. The absence of the reduction peak B when the bridge was used (red curve in Figure 2a) indicates that the gold etching and redeposition effect was effectively inhibited. Nonetheless, it should be mentioned that the sulfuric acid solution might already contain some small amount of chloride impurities. In their rotating ring disk study, Cadle and Bruckenstein[35] estimated a $Cl^-$ concentration of 0.22 $\mu$M for a 0.2 M $H_2SO_4$ solution. Due to the competitive effect of $Cl^-$ adsorption,[35] the voltammogram without a bridge shows a 13 mV anodic shift in the onset potential of gold oxidation and a slight (3 mV) anodic shift in the oxide reduction peaks. To calculate the surface area for the two voltammograms in Figure 2a, we first integrated the oxide reduction current. Peak A with the bridge was integrated using the trapezoidal method, while without the bridge, we used a Lorentzian fit to separate gold reduction from redeposition contribution. eq 2 yielded the surface area for both configurations (Figure 2b). The Bare Au electrode cycled without a bridge exhibited an approximately 10% lower SA, suggesting that chlorides effectively decrease the surface roughness of the electrodes. This assessment is consistent with earlier scanning tunneling microscopy (STM) studies on Au substrates[81,82] which demonstrated enhanced step mobility resulting in smoother terraces when chlorides were present during the formation and reduction of the gold oxide.

*Surface Area Comparison.* In light of the adverse impact of chlorides on Au morphology and SA measurements, all subsequent experiments used a triple junction Ag|AgCl reference with a bridge filled with 0.5 M $H_2SO_4$. Accordingly, we assessed the surface area of three Bare Au electrodes (Figure S2) by integrating the oxide reduction peak on the 20th scan and applying eq 2. These samples exhibited a mean SA of 0.67 ± 0.03 $cm^2$, with a roughness factor of 1.36, consistent with other reports on Au sputtered films on glass.[83]

The minimal intersample variation in SA can be attributed to the highly reproducible microfabrication process. With this reliable baseline established for a gold film on a flat substrate, we applied the same characterization procedure to NS Au, consisting of a thin gold film on a nanostructured support. The comparison of cyclic voltammograms in $H_2SO_4$ for both the Bare Au and NS Au electrodes is presented in Figure 3a. The corresponding computed SA values are depicted in the bar plot in Figure 3b. The calculation was based on three independent NS Au electrodes (Figure S3), resulting in a mean SA of 5.3 ± 0.3 $cm^2$, corresponding to a remarkable roughness factor of 10.8.

*Exposed Facet Evaluation and Surface Energy.* Within the potential range of 1.1 to 1.5 V, three distinct peaks emerge in the forward scan (Figure 3c), each associated with specific crystallographic facets.[84] The first peak, positioned at 1.20 V ± 10 mV, corresponds to the (100) crystal facet. Subsequently, the second peak at 1.27 V ± 10 mV is attributed to the (110) facet, while the third peak at 1.37 V ± 10 mV aligns with the (111) facet. Figure 3c illustrates the CVs of Bare Au and NS Au, normalized to the peak maximum. Remarkably, NS Au displays a heightened (110) component and a diminished (111) contribution compared to Bare Au—while presenting a CV with a shape resembling that of nanoporous Au electrodes.[85,86] To attempt to quantify each contribution, Gaussian components are fitted to each CV on a quadratic baseline. Although widely employed, such a procedure presents some limitations, as summarized by Olaya et al.[86] The resulting peak positions, widths, and areas for three samples of Bare Au and NS Au are detailed in Tables S1 and S2, respectively. At the 20th cycle of Bare Au, the (111) facet dominates, contributing 48% to the total area, followed by (110) at 37% and (100) at 15%. In contrast, NS Au exhibits (110) as the primary peak, constituting 48% of the total area, followed by (111) at 37% and (100) at 17%. Multiplying the facet fraction by the surface energy of each facet[87] provides an overall estimate of the surface energy. NS Au, with a surface energy of 1.77 $J/m^2$, is less thermodynamically stable compared to Bare Au, which exhibits a surface energy of 1.72 $J/m^2$. This difference can be attributed to the reduced fraction of the most stable (111) facet in NS Au compared to Bare Au.

**Electrochemical Sensing of Glucose.** *Incipient Oxide Formation by Electrochemical Activation.* Although seldom mentioned, gold-based non-enzymatic electrochemical glucose sensors always require to be activated, and this can be related to the electrocatalytic nature of gold at neutral pH. In their investigation, Vassilyev et al.[26] proposed the hydrous gold oxide $AuOH_{ads}$ to be the active species due to the pronounced pH dependency of the process. This interpretation aligns well with the Incipient Hydrous Oxide Adatom Mediator (IHOAM) model by Burke,[88,89] which posits that the formation of incipient hydrous oxides in the premonolayer region determines the electrocatalytic properties of gold. The hydrous oxide can be generated by the anodic discharge of water at neutral pH,[90] with electrochemical cycling promoting its formation.[91] Rodríguez-López et al.[92] employed a scanning electrochemical microscope to evaluate and quantify the formed hydrous oxide during cycling in both PBS and Tris-$H_2SO_4$ buffer solutions. However, Wooten et al. later observed that the hydrous oxide formed in the Tris-$H_2SO_4$ buffer was inactive toward glucose,[91] as opposed to the one formed in PBS. The discrepancy was attributed to the specific adsorption of the counterions that block the active sites.

To determine how many cycles were required to complete activation, we cycled Bare Au and NS Au between −0.2 and 1.2 V in 0.1 M PBS with 10 mM glucose at 100 mV/s. The glucose electrooxidation current was observed to increase and eventually stabilize after 30 cycles for Bare Au and 10 cycles for NS Au (Figure S4). Therefore, we determined that 30 cycles in 0.1 M PBS were adequate to attain a stable and active state, and we performed this activation process before each measurement (refer to Figure S5a,b for the cycle-to-cycle


https://doi.org/10.1021/acsomega.4c09270
ACS Omega 2025, 10, 9165−9176

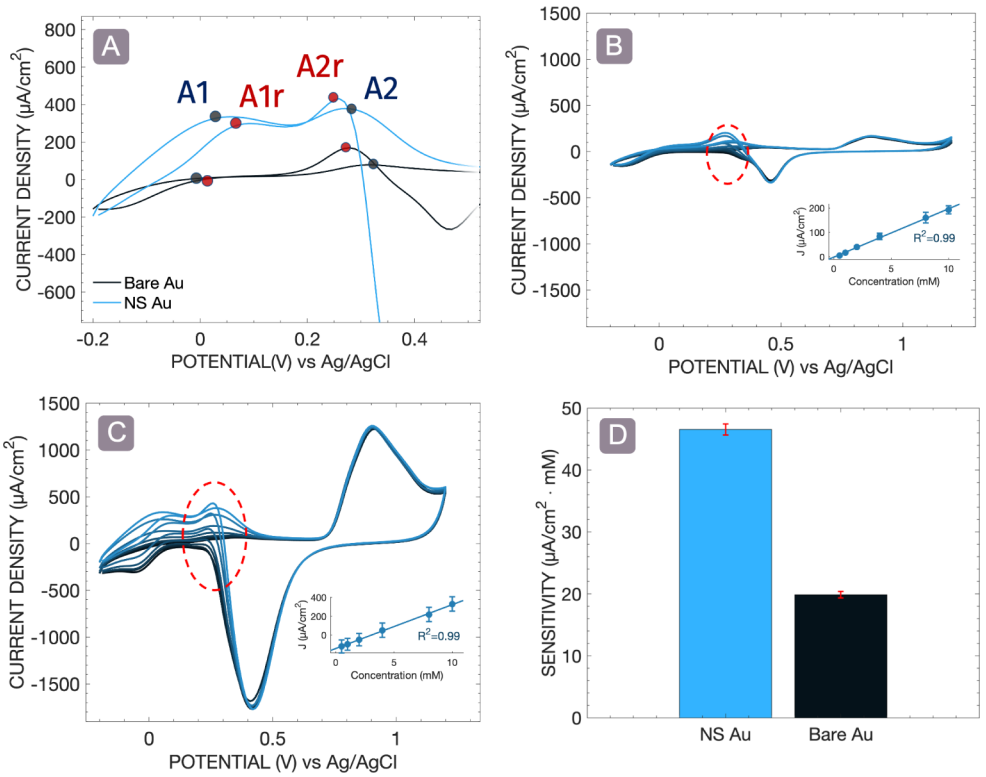


**Figure 4.** (a) Zoomed-in cyclic voltammograms in the region of glucose oxidation for Bare Au (dark blue) and NS Au (light blue) in 0.1 M PBS with 10 mM of glucose. (b) Cyclic voltammetric calibration of Bare Au in 0.1M PBS solution with various concentrations of glucose (0.5 mM, 1 mM, 2 mM, 4 mM, 8 mM, and 10 mM). In the inset, the linear relationship between the peak current density (peak A2r) and the glucose concentration is shown. (c) Cyclic voltammetric calibration of NS Au in 0.1M PBS solution with various concentrations of glucose (0.5, 1, 2, 4, 8, and 10 mM). In the inset, the linear relationship between the peak current density (peak A2r) and the glucose concentration is shown. (d) Bar plot representing the sensitivities of the Bare Au and NS Au electrodes toward glucose. $\nu$ = 100 mV/s. Data are presented as mean ± SD with $n$ = 3.

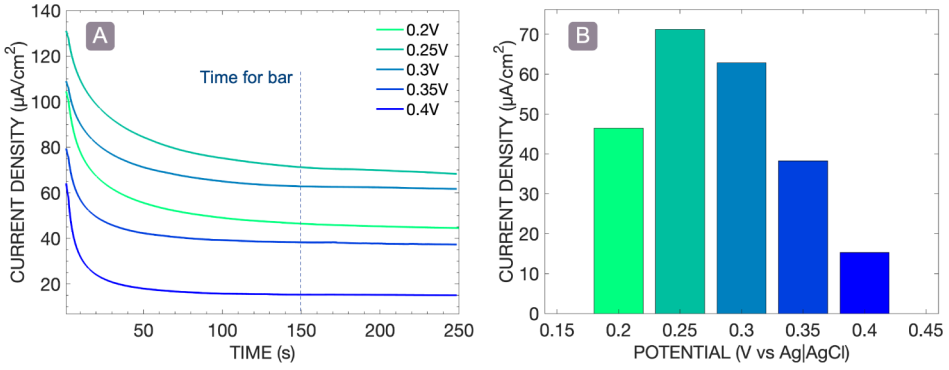


**Figure 5.** (a) Chronoamperometric curves of the Bare Au electrode in 0.1M PBS (6 mM glucose) with a stir bar rotation speed of 375 rpm at an applied potential from 0.2 to 0.4 V in steps of 0.05 V. (b) Bar plot representing the current density at equilibrium (after 150s).

activation voltammograms of Bare Au and NS Au, respectively).

*Cyclic Voltammetric Calibration.* After subjecting the electrodes, both Bare Au and NS Au, to 30 activation cycles, we proceeded to assess their respective glucose-sensing capabilities using cyclic voltammetry (CV).

In Figure 4a, the corresponding voltammograms in 0.1 M PBS with 10 mM glucose are displayed. Intriguingly, four discernible peaks emerge in the case of NS Au electrodes, denoted as A1 at 0.05 V and A2 at 0.3 V during the forward scan, and their counterparts, A1r and A2r, during the backward scan. Conversely, for the Bare Au electrodes, mainly A2 and A2r peaks are observed, with A1 and A1r being little more than a shoulder. It is noteworthy that A1 and A1r, as well as A2 and A2r, correspond to the same redox transition. In their work on single crystal Au electrodes, Hsiao et al.[93] observed how the crystallographic orientation of the exposed Au planes exerts influence over whether a CV exhibits two or four peaks. Accordingly, the CV of Bare Au in PBS in the presence of glucose closely corresponds to that of a single crystal Au (111) electrode. This finding is consistent with our $H_2SO_4$ CV fittings (Figure 3d), which indicated a higher proportion of (111) facets. NS Au exhibits a response reminiscent of Au(110) and Au(100) electrodes, with its characteristic four peaks, as anticipated due to the prevalence of exposed (110) facets in $H_2SO_4$ cycling.



https://doi.org/10.1021/acsomega.4c09270
ACS Omega 2025, 10, 9165−9176

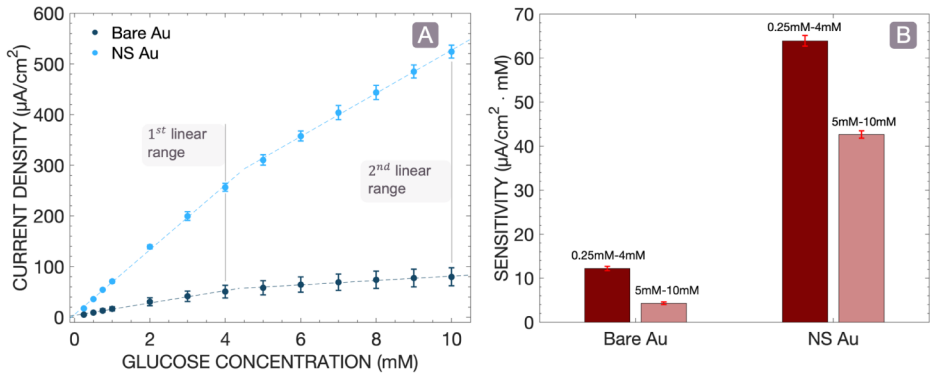


**Figure 6.** (a) Chronoamperometric calibration of the Bare Au and NS Au electrodes in 0.1M PBS solution with a stir bar rotation speed of 375 rpm at an applied potential from 0.25 V. Glucose concentration increased first in 4 steps of 0.25 mM and then in steps of 1 mM until 10 mM. (b) Bar plot comparing the corresponding sensitivities for Bare Au and NS Au in the two observed linear ranges.

**Table 1. Comparison of the Sensing Performance for Bare Au and NS Au Electrodes with Other Au-Based Materials[a]**

| | Potential (V)[b] | Linear Range (mM) | Sensitivity ($\mu$A·cm$^{-2}$·mM$^{-1}$) | LOD ($\mu$M) | ref |
|---|---|---|---|---|---|
| Bare Au | 0.25 | 0.25−4 | 12.2 ± 0.5 | 2.9 | This work |
| | - | 5−10 | 4.3 ± 0.3 | 8.2 | - |
| NS Au | - | 0.25−4 | 63.9 ± 1.2 | 9.9 | - |
| - | - | 5−10 | 42.6 ± 0.8 | 14.8 | - |
| AuNP/GONR/CS | 0.2 | 0.005−4.92 | 59.1 | 5 | 96 |
| | - | 4.92−10 | 31.4 | | |
| AuNP/Gr/GC | 0.45 | 0.5−9 | 1.1 | 55 | 97 |
| Au/LSGE | 0.2 | 0.5−20 | 15.14 | 210 | 98 |
| Au/$TiO_2$ | 0.15 | 0.05−3 | 45 | 50 | 99 |
| AuNT | 0.25 | 0.005−16.4 | 44.2 | 2.1 | 19 |
| Au/$MnO_2$ | 0.2 | 0.5−10 | 13.1 | - | 100 |

[a]The solution is PBS at neutral pH in the absence of chlorides, and the sensitivity is expressed with respect to the geometrical area. [b]Expressed vs. AglAgCl (3 M).

We recorded the CVs in 0.1 M PBS at various glucose concentrations, taken at 0, 0.5, 1, 2, 4, 8, and 10 mM. Subsequently, we produced a calibration plot by expressing the current density of the strongest oxidation peak (A2r both for Bare Au and NS Au) as a function of the glucose concentration. Figure 4b illustrates the cyclic voltammograms obtained in the third cycle for the Bare Au electrode, accompanied by the calibration plot derived from three independent calibrations. Similarly, Figure 4c shows the corresponding data for the NS Au electrode based on three independent calibrations. Figure 4d provides a direct comparison of the sensitivity between the NS Au and Bare Au electrodes. Both NS Au and Bare Au displayed very good linearity ($R^2$ = 0.99) within the 1−10 mM range of glucose concentration. Specifically, Bare Au showed a sensitivity of 19.85 ± 0.52 $\mu$A·cm$^{-2}$·mM$^{-1}$ and NS Au 46.54 ± 0.89 $\mu$A·cm$^{-2}$·mM$^{-1}$.

*Chronoamperometric Calibration.* While cyclic voltammetry offers valuable insights, its use as an analytical technique is limited by its inherent semiquantitative nature. This is primarily because distinguishing faradaic from nonfaradaic components can be challenging.[94] As a result, the characterization of the sensors was complemented with a chronoamperometric calibration. To achieve the maximum current density with the microfabricated electrodes, it was first necessary to optimize the applied potential. For this purpose, the chronoamperometric response of the Bare Au electrode in a 0.1 M PBS solution containing 6 mM glucose was recorded under stirring conditions. The applied potentials were varied from 0.2 to 0.4 V in 0.05 V increments, as illustrated in Figure 5a. Subsequently, after allowing for sufficient equilibration time (150 s), the current density was evaluated and expressed as a function of the applied potential in the bar plot presented in Figure 5b. As expected, the highest current density was observed at 0.25 V. This potential coincides with position A2r, corresponding to the most intense peak in cyclic voltammetry, as shown in Figure 4a.

The optimized potential for Bare Au was extended to NS Au, as its main peak in CV (A2r) lay at a similar potential. The following experiments were thus conducted under continuous stirring (375 rpm) at a fixed applied potential of 0.25 V (vs Agl AgCl) with the addition of 0.25 mM glucose until 1 mM and then in steps of 1 mM until 10 mM. Based on the chronoamperometric curves (Figure S6), a calibration plot was produced by averaging the value of the current density in the middle 10 s for each 30 s step, in order to minimize fluctuations. The result of three independent calibration experiments for both Bare Au and NS Au is shown in Figure 6a. The sensitivity in the 0.25−4 mM range was 12.2 ± 0.5 $\mu$A·cm$^{-2}$·mM$^{-1}$ and 63.9 ± 1.2 $\mu$A·cm$^{-2}$·mM$^{-1}$ for Au Bare and NS Bare, respectively. On the other hand, the sensitivity in the 5−10 mM glucose concentration was 4.3 ± 0.3 $\mu$A·cm$^{-2}$·mM$^{-1}$ and 42.6 ± 0.8 $\mu$A·cm$^{-2}$·mM$^{-1}$ for Bare Au and NS Au, respectively. Notably, a high coefficient of determination $R^2$ = 0.99 was obtained for all linear interpolations. We conducted an accuracy assessment by evaluating the linear relationship between the observed concentrations and the concentrations estimated from linear fits. Figure S8 shows the estimated


https://doi.org/10.1021/acsomega.4c09270
ACS Omega 2025, 10, 9165−9176

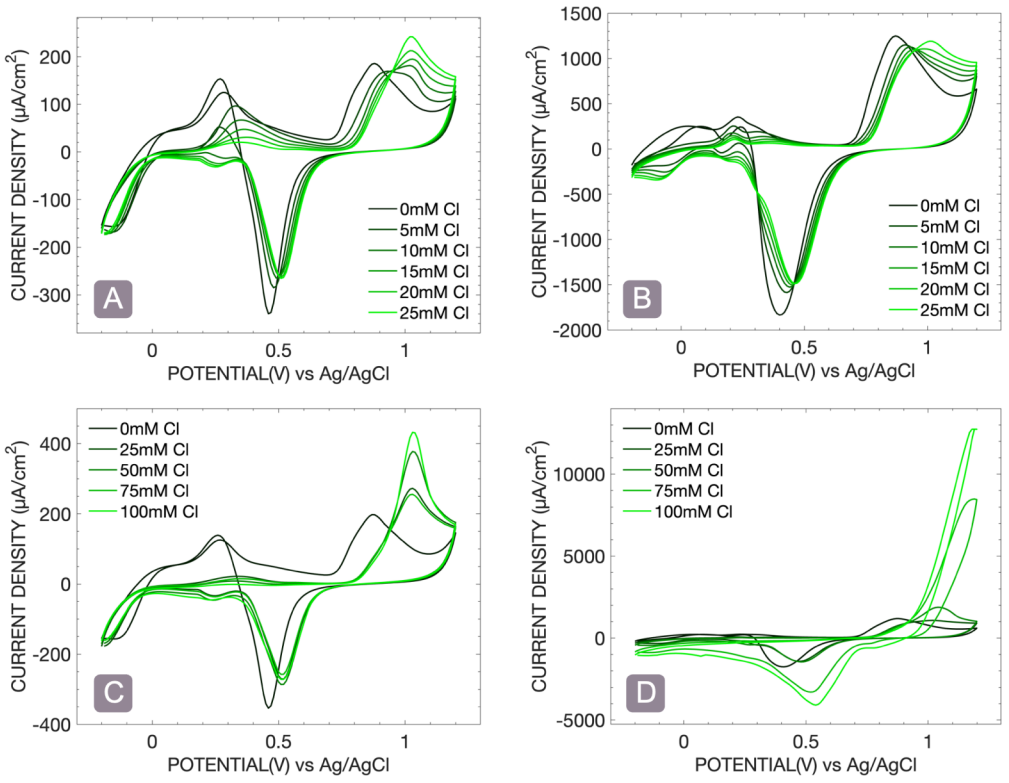


**Figure 7.** Cyclic voltammograms with 6 mM glucose in 0.1 M PBS for chloride concentrations increased in steps of 5 mM until 25 mM for Bare Au (a) and for NS Au (b). Cyclic voltammograms with 6 mM glucose in 0.1 M PBS for chloride concentrations increased in steps of 25 mM until 100 mM for Bare Au (c) and for NS Au (d). $\nu$ = 100 mV/s.

concentrations versus the actual concentrations for the two linear ranges of Bare Au and NS Au, with an overlaid linear regression line. For NSAu, the slope of the plot was 0.99 in both linear ranges, indicating strong agreement between the estimated and observed concentrations. In contrast, Bare Au showed a slope of 0.99 for the first linear range but the slope decreased to 0.96 in the second range, suggesting a slight deviation from linearity as the concentration increased. It should be noted that the sensitivity increase from Bare Au to NS Au scales with a factor of 5 and 10 for the first and second linear ranges, respectively, similar to the increase in ESA (factor 8).

The limit of detection (LOD) was calculated using the following formula:[95]

$$\mathrm{LOD} = \frac{3.3 \cdot \sigma_{\mathrm{blank}}}{S} \tag{5}$$

where $S$ is the sensitivity and $\sigma_{\mathrm{blank}}$ corresponds to the standard deviation for three samples of the mean current density from 40 s to 45 s after polarization, prior to the first glucose addition. For Bare Au, the LOD in the 0.25−4 mM and 5−10 mM ranges is 2.9 $\mu$M and 8.2 $\mu$M. For NS Au, the LOD in the 0.25−3 mM and 4−10 mM ranges is 9.9 $\mu$M and 14.8 $\mu$M. Table 1 summarizes the calculated sensitivity and LOD for Bare Au and NS Au in the observed linear ranges and compares them with other Au-based sensing platforms proposed in the literature. Although not exhaustive, Table 1 clearly demonstrates that our proposed system competes favorably with electrodes modified by using more time-consuming methods, such as wet chemistry synthesized nanoparticles.

**Chloride Resistance.** The work by Makovos et al.[101] and subsequently by Pasta et al.[102] has underscored the adverse impact of chlorides on gold electrodes used in glucose sensing. As previously discussed, Au catalysts necessitate a preliminary CV cycling step before sensing (Figure S4). Hence, it is desirable to explore the chloride resistance of Au-based catalysts within the same potential range. Accordingly, CV experiments were conducted in a 0.1 M PBS solution containing a physiological concentration of glucose (6 mM), with varying chloride concentrations.

We first examined the effect of chlorides by incrementally increasing their concentration in 5 mM intervals for Bare Au (Figure 7a) and NS Au (Figure 7b). As chlorides are added, their specific adsorption competes with the oxide formation, progressively leading to (1) an anodic shift of the gold oxide onset potential, (2) the rise of a gold dissolution peak at ≈1 V, (3) an anodic shift and intensity reduction of the gold reduction peak at 0.4 V, and finally, (4) a notable reduction of the glucose electrooxidation peak.

Already at 5 mM $Cl^-$, a substantial current drop was observed for all glucose peaks (A1, A2, A1r, and A2r shown in Figure 4). Specifically, peak A2r (Figure 4a), the most prominent peak, exhibited a high susceptibility to chlorides, decreasing by 66% for Bare Au and 73% for NS Au. The smaller return peak A1r witnessed an even more significant current decrease: a complete loss of signal for Bare Au and a 91% reduction for NS Au. Similarly, peak A1 also virtually disappeared, experiencing a 90% signal loss for Bare Au and a 76% reduction for NS Au. In contrast, the forward peak A2 appeared to be relatively more resilient to chloride adsorption, with only a 23% reduction for Bare Au and 28% for NS Au. Although for $Cl^-$ < 25 mM, NS Au and Bare Au behaved


https://doi.org/10.1021/acsomega.4c09270
ACS Omega 2025, 10, 9165−9176

similarly, when increasing the $Cl^-$ concentration in steps of 25 mM until 100 mM (Figure 7c,d) the NS Au electrode saw significantly greater rates of electrochemical dissolution compared to Bare Au. This difference may be attributed to the greater fraction of (111) facets on Bare Au, which are characterized by a lower surface energy and work function in comparison to the (110) and (100) facets. Based on these findings, a number of more sophisticated strategies should be investigated, such as optimizing the potential windows of activation to minimize material dissolution, investigating various surface modification techniques to enhance crystal facet formation, exploring barrier methods to mitigate material degradation in corrosive environments, and researching alternative materials for improved durability and stability.

## CONCLUSIONS

This investigation highlights the potential of employing femtosecond laser-treated glass, coupled with a deposition of a thin gold layer, as a promising strategy to fabricate nanostructured electrodes for glucose sensing applications. The resultant microchip-compatible platform exhibits significant improvements in sensitivity compared with conventional flat gold film electrodes. Specifically, it demonstrates 5-fold and 10-fold greater sensitivities in the 0.25 mM−4 mM and 5 mM−10 mM ranges, respectively. This enhanced performance is attributed to a substantial increase (approximately 8-fold) in the electroactive area facilitated by the laser nanostructuration of the glass surface. The samples were calibrated using cyclic voltammetry and chronoamperometry, and a deliberate effort was made to perform experiments with a AglAgCl reference electrode, given its widespread use in integrated sensors. To address the potential impact of chloride leakage on the surface area estimation and overall glucose response, the use of a salt bridge was considered necessary. A thorough investigation into chloride resistance was conducted under realistic conditions, involving cyclic activation in the −0.2 to 1.2 V range. The findings revealed that a gradual deactivation of both Bare Au and NS Au as Cl concentrations increased. At physiological $Cl^-$ levels (100 mM), both electrodes exhibited noticeable etching with a more pronounced effect on NS Au. Despite both samples being polycrystalline, the exposed planes of the film are suggested to account for the observed differences, with the more stable (111) crystal facet affording the greatest resistance to dissolution. Various methods, including anodization, could be explored to selectively enhance one plane over the other. In summary, this research lays a robust foundation for the development of integrated nonenzymatic glucose sensors, with potential applications in broader fields such as electrocatalysis and sensing, where high-surface-area electrodes are advantageous. Future endeavors will evaluate the sensing performance at different pH and on mitigating chloride poisoning through a variety of methods, such as employing membranes, narrowing the potential activation window, or combining with other materials for improved stability.

## ASSOCIATED CONTENT

### Supporting Information

The Supporting Information is available free of charge at https://pubs.acs.org/doi/10.1021/acsomega.4c09270.

Cyclic voltammograms for electrode activation and electrode area determination, along with X-ray diffraction patterns, chronoamperograms, and accuracy assessments (PDF)

## AUTHOR INFORMATION


### Corresponding Author

**Filippo Franceschini** − *KU Leuven, Department of Physics and Astronomy (HF), Leuven 3001, Belgium;* orcid.org/0000-0001-7208-781X; Email: filippo.franceschini@kuleuven.be

### Authors

**Balasubramanian Nagarajan** − *KU Leuven, Department of Mechanical Engineering, Leuven 3001, Belgium; Flanders Make@KU Leuven, Leuven 3001, Belgium*

**Iliana Claes** − *KU Leuven, Department of Physics and Astronomy (HF), Leuven 3001, Belgium*

**Olivier Deschaume** − *KU Leuven, Department of Physics and Astronomy (Soft Matter and Biophysics), Leuven 3001, Belgium;* orcid.org/0000-0001-6222-0947

**Carmen Bartic** − *KU Leuven, Department of Physics and Astronomy (Soft Matter and Biophysics), Leuven 3001, Belgium;* orcid.org/0000-0001-9577-2844

**Sylvie Castagne** − *KU Leuven, Department of Mechanical Engineering, Leuven 3001, Belgium; Flanders Make@KU Leuven, Leuven 3001, Belgium*

**Irene Taurino** − *KU Leuven, Department of Physics and Astronomy (HF), Leuven 3001, Belgium; KU Leuven, Department of Electrical Engineering(ESAT-MNS), Leuven 3001, Belgium*

Complete contact information is available at: https://pubs.acs.org/10.1021/acsomega.4c09270


### Notes

The authors declare no competing financial interest.

## ACKNOWLEDGMENTS

The authors acknowledge the financial support from the Fonds Wetenschappelijk Onderzoek - Vlaanderen (FWO) through the Medium-Scale Research Infrastructure project FemtoFac I001120N. F.F. acknowledges the support of the Research Foundation Flanders (FWO) for the PhD fellowship 1S61723N.

## REFERENCES


(1) American Diabetes Association. Diagnosis and Classification of Diabetes Mellitus. *Diabetes Care* **2014**, *37*, S81−S90.

(2) Clark, L. C., Jr.; Lyons, C. Electrode systems for continuous monitoring in cardiovascular surgery. *Ann. N. Y. Acad. Sci.* **1962**, *102*, 29−45.

(3) Scheller, F. W.; Schubert, F.; Neumann, B.; Pfeiffer, D.; Hintsche, R.; Dransfeld, I.; Wollenberger, U.; Renneberg, R.; Warsinke, A.; Johansson, G.; Skoog, M.; Yang, X.; Bogdanovskaya, V.; Bückmann, A.; Zaitsev, S. Second generation biosensors. *Biosens. Bioelectron.* **1991**, *6*, 245−253.

(4) Juska, V. B.; Pemble, M. E. A Critical Review of Electrochemical Glucose Sensing: Evolution of Biosensor Platforms Based on Advanced Nanosystems. *Sensors* **2020**, *20*, 6013.

(5) Teymourian, H.; Barfidokht, A.; Wang, J. Electrochemical glucose sensors in diabetes management: an updated review (2010−2020). *Chem. Soc. Rev.* **2020**, *49*, 7671−7709.

(6) Hwang, D. W.; Lee, S.; Seo, M.; Chung, T. D. Recent advances in electrochemical non-enzymatic glucose sensors - A review. *Anal. Chim. Acta* **2018**, *1033*, 1−34.

(7) Wei, M.; Qiao, Y.; Zhao, H.; Liang, J.; Li, T.; Luo, Y.; Lu, S.; Shi, X.; Lu, W.; Sun, X. Electrochemical non-enzymatic glucose sensors: recent progress and perspectives. *Chem. Commun.* **2020**, *56*, 14553−14569.
(8) Chen, T.; Liu, D.; Lu, W.; Wang, K.; Du, G.; Asiri, A. M.; Sun, X. Three-Dimensional Ni2P Nanoarray: An Efficient Catalyst Electrode for Sensitive and Selective Nonenzymatic Glucose Sensing with High Specificity. *Anal. Chem.* **2016**, *88*, 7885−7889.
(9) Aun, T. T.; Salleh, N. M.; Ali, U. F. M.; Manan, N. S. A. Non-Enzymatic Glucose Sensors Involving Copper: An Electrochemical Perspective. *Crit. Rev. Anal. Chem.* **2023**, *53* (3), 537−593.
(10) Qiao, Y.; Liu, Q.; Lu, S.; Chen, G.; Gao, S.; Lu, W.; Sun, X. High-performance non-enzymatic glucose detection: using a conductive Ni-MOF as an electrocatalyst. *J. Mater. Chem. B* **2020**, *8*, 5411−5415.
(11) Wu, P.; Fan, J.; Tai, Y.; He, X.; Zheng, D.; Yao, Y.; Sun, S.; Ying, B.; Luo, Y.; Hu, W.; Sun, X.; Li, Y. Ag@TiO2 nanoribbon array: a high-performance sensor for electrochemical non-enzymatic glucose detection in beverage sample. *Food Chem.* **2024**, *447*, 139018.
(12) Nugba, B. E.; El-Moneim, A. A.; Mousa, N. O.; Osman, A. A nonenzymatic laser-induced flexible amperometric graphene electrode for glucose detection in saliva. *Carbon Lett.* **2023**, *33*, 1767−1780.
(13) Ding, Y.; Wang, Y.; Su, L.; Bellagamba, M.; Zhang, H.; Lei, Y. Electrospun Co3O4 nanofibers for sensitive and selective glucose detection. *Biosens. Bioelectron.* **2010**, *26*, 542−548.
(14) Franceschini, F.; Taurino, I. Nickel-based catalysts for non-enzymatic electrochemical sensing of glucose: A review. *Phys. Medi.* **2022**, *14*, 100054.
(15) Wu, P.; Yang, J.; Tai, Y.; He, X.; Zhang, L.; Fan, J.; Yao, Y.; Ying, B.; Hu, W. W.; Luo, F.; Sun, X.; Li, Y. Ni@TiO 2 nanoribbon array electrode for high-efficiency non-enzymatic glucose biosensing. *J. Mater. Chem. B* **2024**, *12*, 8897−8901.
(16) Franceschini, F.; Payo, M. R.; Schouteden, K.; Ustarroz, J.; Locquet, J. P.; Taurino, I. MBE Grown Vanadium Oxide Thin Films for Enhanced Non-Enzymatic Glucose Sensing. *Adv. Funct. Mater.* **2023**, *33* (43), 2304037.
(17) Kim, S. H.; Choi, J. B.; Nguyen, Q. N.; Lee, J. M.; Park, S.; Chung, T. D.; Byun, J. Y. Nanoporous platinum thin films synthesized by electrochemical dealloying for nonenzymatic glucose detection. *Phys. Chem. Chem. Phys.* **2013**, *15*, 5782−5787.
(18) Weremfo, A.; Fong, S. T. C.; Khan, A.; Hibbert, D. B.; Zhao, C. Electrochemically roughened nanoporous platinum electrodes for non-enzymatic glucose sensors. *Electrochim. Acta* **2017**, *231*, 20−26.
(19) Tian, T.; Dong, J.; Xu, J. Direct electrodeposition of highly ordered gold nanotube arrays for use in non-enzymatic amperometric sensing of glucose. *Microchim. Acta* **2016**, *183*, 1925−1932.
(20) Shen, L.; Liang, Z.; Chen, Z.; Wu, C.; Hu, X.; Zhang, J.; Jiang, Q.; Wang, Y. Reusable electrochemical non-enzymatic glucose sensors based on Au-inlaid nanocages. *Nano Res.* **2022**, *15*, 6490−6499.
(21) Wang, J.; Cao, X.; Wang, X.; Yang, S.; Wang, R. Electrochemical Oxidation and Determination of Glucose in Alkaline Media Based on Au (111)-Like Nanoparticle Array on Indium Tin Oxide Electrode. *Electrochim. Acta* **2014**, *138*, 174−186.
(22) Ye, J.-S.; Chen, C.-W.; Lee, C.-L. Pd nanocube as non-enzymatic glucose sensor. *Sens. Actuators, B* **2015**, *208*, 569−574.
(23) Cai, Z.-x.; Liu, C.-c.; Wu, G.-h.; Chen, X.-m.; Chen, X. Palladium nanoparticles deposit on multi-walled carbon nanotubes and their catalytic applications for electrooxidation of ethanol and glucose. *Electrochim. Acta* **2013**, *112*, 756−762.
(24) Elkholy, A. E.; Heakal, F. E.-T.; El-Said, W. A. Improving the electrocatalytic performance of Pd nanoparticles supported on indium/tin oxide substrates towards glucose oxidation. *Appl. Catal., A* **2019**, *580*, 28−33.
(25) Dong, Q.; Song, D.; Huang, Y.; Xu, Z.; Chapman, J. H.; Willis, W. S.; Li, B.; Lei, Y. High-temperature annealing enabled iridium oxide nanofibers for both non-enzymatic glucose and solid-state pH sensing. *Electrochim. Acta* **2018**, *281*, 117−126.
(26) Vassilyev, Y.; Khazova, O.; Nikolaeva, N. Kinetics and mechanism of glucose electrooxidation on different electrode-catalysts Part II. Effect of the nature of the electrode and the electrooxidation mechanism. *J. Electroanal. Chem. Interfacial Electrochem.* **1985**, *196*, 127−144.
(27) Hammer, B.; Nørskov, J. Electronic factors determining the reactivity of metal surfaces. *Surf. Sci.* **1995**, *343*, 211−220.
(28) Toghill, K. E.; Compton, R. G. Electrochemical Non-enzymatic Glucose Sensors: A Perspective and an Evaluation. *Int. J. Electrochem. Sci.* **2010**, *5*, 1246−1301.
(29) Xia, Y.; Huang, W.; Zheng, J.; Niu, Z.; Li, Z. Nonenzymatic amperometric response of glucose on a nanoporous gold film electrode fabricated by a rapid and simple electrochemical method. *Biosens. Bioelectron.* **2011**, *26*, 3555−3561.
(30) Shu, H.; Chang, G.; Su, J.; Cao, L.; Huang, Q.; Zhang, Y.; Xia, T.; He, Y. Single-step electrochemical deposition of high performance Au-graphene nanocomposites for nonenzymatic glucose sensing. *Sens. Actuators, B* **2015**, *220*, 331−339.
(31) Xu, F.; Cui, K.; Sun, Y.; Guo, C.; Liu, Z.; Zhang, Y.; Shi, Y.; Li, Z. Facile synthesis of urchin-like gold submicrostructures for nonenzymatic glucose sensing. *Talanta* **2010**, *82*, 1845−1852.
(32) Li, Y.; Song, Y.-Y.; Yang, C.; Xia, X.-H. Hydrogen bubble dynamic template synthesis of porous gold for nonenzymatic electrochemical detection of glucose. *Electrochem. Commun.* **2007**, *9*, 981−988.
(33) Hanssen, B. L.; Siraj, S.; Wong, D. K. Recent strategies to minimise fouling in electrochemical detection systems. *Rev. Anal. Chem.* **2016**, *35*, 1−28.
(34) Szunerits, S.; Pagneux, Q.; M'Barek, Y. B.; Vassal, S.; Boukherroub, R. Do not let electrode fouling be the enemy of bioanalysis. *Bioelectrochemistry* **2023**, *153*, 108479.
(35) Cadle, S.; Bruckenstein, S. A ring-disk study of the effect of trace chloride ion on the anodic behavior of gold in 0.2 M H2SO4. *J. Electroanal. Chem. Interfacial Electrochem.* **1973**, *48*, 325−331.
(36) Ye, S.; Ishibashi, C.; Shimazu, K.; Uosaki, K. An In Situ Electrochemical Quartz Crystal Microbalance Study of the Dissolution Process of a Gold Electrode in Perchloric Acid Solution Containing Chloride Ion. *J. Electrochem. Soc.* **1998**, *145*, 1614−1623.
(37) Hong, X.; Tan, C.; Chen, J.; Xu, Z.; Zhang, H. Synthesis, properties and applications of one- and two-dimensional gold nanostructures. *Nano Res.* **2015**, *8*, 40−55.
(38) Taurino, I.; Sanzò, G.; Antiochia, R.; Tortolini, C.; Mazzei, F.; Favero, G.; De Micheli, G.; Carrara, S. Recent advances in Third Generation Biosensors based on Au and Pt Nanostructured Electrodes. *TrAC, Trends Anal. Chem.* **2016**, *79*, 151−159.
(39) Tien, J.; Terfort, A.; Whitesides, G. M. Microfabrication through Electrostatic Self-Assembly. *Langmuir* **1997**, *13*, 5349−5355.
(40) Wang, L.; Bai, J.; Huang, P.; Wang, H.; Zhang, L.; Zhao, Y. Self-assembly of gold nanoparticles for the voltammetric sensing of epinephrine. *Electrochem. Commun.* **2006**, *8*, 1035−1040.
(41) Di, J.; Shen, C.; Peng, S.; Tu, Y.; Li, S. A one-step method to construct a third-generation biosensor based on horseradish peroxidase and gold nanoparticles embedded in silica sol-gel network on gold modified electrode. *Anal. Chim. Acta* **2005**, *553*, 196−200.
(42) Sutanto, J.; Smith, R. L.; Collins, S. D. Fabrication of nano-gap electrodes and nano wires using an electrochemical and chemical etching technique. *J. Micromech. Microeng.* **2010**, *20*, 045016.
(43) Brenner, A. *Electrodeposition of alloys: principles and practice*; Elsevier, 2013.
(44) Li, Q.; Wang, Q.; Li, L.; Yang, L.; Wang, Y.; Wang, X.; Fang, H.-T. Femtosecond Laser-Etched MXene Microsupercapacitors with Double-Side Configuration via Arbitrary On- and Through-Substrate Connections. *Adv. Energy Mater.* **2020**, *10* (24), 2000470.
(45) Wu, Z.; Yin, K.; Wu, J.; Zhu, Z.; Duan, J.-A.; He, J. Recent advances in femtosecond laser-structured Janus membranes with asymmetric surface wettability. *Nanoscale* **2021**, *13*, 2209−2226.
(46) Bai, X.; Yang, Q.; Fang, Y.; Zhang, J.; Yong, J.; Hou, X.; Chen, F. Superhydrophobicity-memory surfaces prepared by a femtosecond laser. *Chem. Eng. J.* **2020**, *383*, 123143.
(47) Jiang, S.; Hu, Y.; Wu, H.; Zhang, Y.; Zhang, Y.; Wang, Y.; Zhang, Y.; Zhu, W.; Li, J.; Wu, D.; Chu, J. Multifunctional Janus


https://doi.org/10.1021/acsomega.4c09270
*ACS Omega* 2025, 10, 9165−9176

Microplates Arrays Actuated by Magnetic Fields for Water/Light Switches and Bio-Inspired Assimilatory Coloration. *Adv. Mater.* **2019**, *31* (15), No. e1807507.
(48) Chang, H.-W.; Chen, C.-L.; Jhu, S.-J.; Lin, G.-W.; Cheng, C.-W.; Tsai, Y.-C. Femtosecond laser structuring in the fabrication of periodic nanostructure on titanium for enhanced photoelectrochemical dopamine sensing performance. *Microchem. J.* **2023**, *187*, 108423.
(49) Wang, S.; Jiang, L.; Hu, J.; Wang, Q.; Zhan, S.; Lu, Y. Dual-functional CuxO/Cu electrodes for supercapacitors and non-enzymatic glucose sensors fabricated by femtosecond laser enhanced thermal oxidation. *J. Alloys Compd.* **2020**, *815*, 152105.
(50) Beltrán, A. M.; Giner, M.; Rodríguez, A.; Trueba, P.; Rodríguez-Albelo, L. M.; Vázquez-Gámez, M. A.; Godinho, V.; Alcudia, A.; Amado, J. M.; López-Santos, C.; Torres, Y. Influence of Femtosecond Laser Modification on Biomechanical and Biofunctional Behavior of Porous Titanium Substrates. *Materials* **2022**, *15*, 2969.
(51) Wu, T.; Wu, Z.; He, Y.; Zhu, Z.; Wang, L.; Yin, K. Femtosecond laser textured porous nanowire structured glass for enhanced thermal imaging. *Chin. Opt. Lett.* **2022**, *20*, 033801.
(52) Fang, Z.; Cheng, Y.; Yang, Q.; Lu, Y.; Zhang, C.; Li, M.; Du, B.; Hou, X.; Chen, F. Design of Metal-Based Slippery Liquid-Infused Porous Surfaces (SLIPSs) with Effective Liquid Repellency Achieved with a Femtosecond Laser. *Micromachines* **2022**, *13*, 1160.
(53) Indrišiūnas, S.; Svirplys, E.; Gedvilas, M. Large-Area Fabrication of LIPSS for Wetting Control Using Multi-Parallel Femtosecond Laser Processing. *Materials* **2022**, *15* (16), 5534.
(54) Yong, J.; Yang, Q.; Hou, X.; Chen, F. Nature-Inspired Superwettability Achieved by Femtosecond Lasers. *Ultrafast Sci.* **2022**, *2022*, 9895418.
(55) Gattass, R. R.; Mazur, E. Femtosecond laser micromachining in transparent materials. *Nat. Photonics* **2008**, *2*, 219−225.
(56) Valle, G. D.; Osellame, R.; Laporta, P. Micromachining of photonic devices by femtosecond laser pulses. *J. Opt. A: Pure Appl. Opt.* **2009**, *11* (1), 013001.
(57) Xu, B.-B.; Zhang, Y.-L.; Xia, H.; Dong, W.-F.; Ding, H.; Sun, H.-B. Fabrication and multifunction integration of microfluidic chips by femtosecond laser direct writing. *Lab Chip* **2013**, *13*, 1677−1690.
(58) Yong, J.; Zhan, Z.; Singh, S. C.; Chen, F.; Guo, C. Microfluidic Channels Fabrication Based on Underwater Superpolymphobic Microgrooves Produced by Femtosecond Laser Direct Writing. *ACS Appl. Polym. Mater.* **2019**, *1*, 2819−2825.
(59) Gao, X.; Feng, W.; Zhu, Z.; Wu, Z.; Li, S.; Kan, S.; Qiu, X.; Guo, A.; Chen, W.; Yin, K. Rapid Fabrication of Superhydrophilic Micro/Nanostructured Nickel Foam Toward High-Performance Glucose Sensor. *Adv. Mater. Interfaces* **2021**, *8* (7), 2002133.
(60) Chen, J.; Liu, G.; Feng, W.; Bu, M.; Zhu, Z.; Gao, X.; Huang, S.; Deng, L. Laser ablation enhancing the electrochemical sensing performance of copper foam toward glucose. *Chin. J. Anal. Chem.* **2021**, *49*, 75−80.
(61) Nečas, D.; Klapetek, P. Gwyddion: an open-source software for SPM data analysis. *Cent. Eur. J. Phys.* **2012**, *10*, 181−188.
(62) Orazi, L.; Romoli, L.; Schmidt, M.; Li, L. Ultrafast laser manufacturing: from physics to industrial applications. *CIRP Annals* **2021**, *70*, 543−566.
(63) Li, X.; Guan, Y. Theoretical fundamentals of short pulse laser-metal interaction: A review. *Nanotechnol. Precis. Eng.* **2020**, *3*, 105−125.
(64) Shin, H.; Kim, D. Cutting thin glass by femtosecond laser ablation. *Opt. Laser Technol.* **2018**, *102*, 1−11.
(65) Siegel, J.; Lyutakov, O.; Rybka, V.; Kolská, Z.; švorčík, V. Properties of gold nanostructures sputtered on glass. *Nanoscale Res. Lett.* **2011**, *6* (1), 96.
(66) Wyckoff, R. W. G. *Crystal Structures - Vol. 1*, 2nd ed. Interscience Publishers New York: New York, 1963.
(67) Nzulu, G.; Eklund, P.; Magnuson, M. Characterization and identification of Au pathfinder minerals from an artisanal mine site using X-ray diffraction. *J. Mater. Sci.* **2021**, *56*, 7659−7669.
(68) Chen, G.; Hui, P.; Pita, K.; Hing, P.; Kong, L. Conductivity drop and crystallites redistribution in gold film. *Appl. Phys. A. Sci.* **2005**, *80*, 659−665.
(69) Cheng, T.-M.; Huang, T.-K.; Lin, H.-K.; Tung, S.-P.; Chen, Y.-L.; Lee, C.-Y.; Chiu, H.-T. (110)-Exposed Gold Nanocoral Electrode as Low Onset Potential Selective Glucose Sensor. *ACS Appl. Mater. Interfaces* **2010**, *2*, 2773−2780.
(70) Andoralov, V. M.; Tarasevich, M. R.; Tripachev, O. V. Oxygen reduction reaction on polycrystalline gold. Pathways of hydrogen peroxide transformation in the acidic medium. *Russ. J. Electrochem.* **2011**, *47*, 1327−1336.
(71) Fischer, L. M.; Tenje, M.; Heiskanen, A. R.; Masuda, N.; Castillo, J.; Bentien, A.; émneus, J.; Jakobsen, M. H.; Boisen, A. Gold cleaning methods for electrochemical detection applications. *Microelectron. Eng.* **2009**, *86*, 1282−1285.
(72) Noh, M. F. M.; Tothill, I. E. Development and characterisation of disposable gold electrodes, and their use for lead(II) analysis. *Anal. Bioanal. Chem.* **2006**, *386*, 2095−2106.
(73) Spégel, C.; Heiskanen, A.; Acklid, J.; Wolff, A.; Taboryski, R.; Emnéus, J.; Ruzgas, T. On-Chip Determination of Dopamine Exocytosis Using Mercaptopropionic Acid Modified Microelectrodes. *Electroanalysis* **2007**, *19*, 263−271.
(74) Das, S. K.; Nayak, K. K.; Krishnaswamy, P. R.; Kumar, V.; Bhat, N. Review—Electrochemistry and Other Emerging Technologies for Continuous Glucose Monitoring Devices. *ECS Sens. Plus* **2022**, *1* (3), 031601.
(75) Tian, M.; Pell, W. G.; Conway, B. E. EQCN study of anodic dissolution and surface oxide film formation at Au in the presence of Cl- or Br- ions: A model process for corrosion studies. *Corros. Sci.* **2008**, *50*, 2682−2690.
(76) Xu, X.; Makaraviciute, A.; Pettersson, J.; Zhang, S.-L.; Nyholm, L.; Zhang, Z. Revisiting the factors influencing gold electrodes prepared using cyclic voltammetry. *Sens. Actuators, B* **2019**, *283*, 146−153.
(77) Dean, J.; Lange, N. *Lange's Handbook of Chemistry; Lange's handbook of chemistry*; McGraw-Hill, 1999; Vol. *15*.
(78) Gallego, J. H.; Castellano, C.; Calandra, A.; Arvia, A. The electrochemistry of gold in acid aqueous solutions containing chloride ions. *J. Electroanal. Chem. Interfacial Electrochem.* **1975**, *66*, 207−230.
(79) Kasian, O.; Kulyk, N.; Mingers, A.; Zeradjanin, A. R.; Mayrhofer, K. J.; Cherevko, S. Electrochemical dissolution of gold in presence of chloride and bromide traces studied by on-line electrochemical inductively coupled plasma mass spectrometry. *Electrochim. Acta* **2016**, *222*, 1056−1063.
(80) Heumann, T.; Panesar, H. S. Beitrag zur Frage nach dem Auflösungsmechanismus von Gold zu Chlorkomplexen und nach seiner Passivierung. *J. Phys. Chem.* **1965**, *229O*, 84−97.
(81) Trevor, D. J.; Chidsey, C. E. D.; Loiacono, D. N. In Situ Scanning-Tunneling-Microscope Observation of Roughening, Annealing, and Dissolution of Gold (111) in an Electrochemical Cell. *Phys. Rev. Lett.* **1989**, *62*, 929−932.
(82) Honbo, H.; Sugawara, S.; Itaya, K. Detailed in-situ scanning tunneling microscopy of single crystal planes of gold(111) in aqueous solutions. *Anal. Chem.* **1990**, *62*, 2424−2429.
(83) Carolus, M. D.; Bernasek, S. L.; Schwartz, J. Measuring the Surface Roughness of Sputtered Coatings by Microgravimetry. *Langmuir* **2005**, *21*, 4236−4239.
(84) Štrbac, S.; Adžić, R.; Hamelin, A. Oxide formation on gold single crystal stepped surfaces. *J. Electroanal. Chem. Interfacial Electrochem.* **1988**, *249*, 291−310.
(85) Wang, Z.; Ning, S.; Liu, P.; Ding, Y.; Hirata, A.; Fujita, T.; Chen, M. Tuning Surface Structure of 3D Nanoporous Gold by Surfactant-Free Electrochemical Potential Cycling. *Adv. Mater.* **2017**, *29* (41), 1703601.
(86) Olaya, A. R. S.; Zandersons, B.; Wittstock, G. Restructuring of Nanoporous Gold Surfaces During Electrochemical Cycling in Acidic and Alkaline Media. *ChemElectrochem* **2020**, *7*, 3670−3678.
(87) Jiang, Q.; Lu, H. Size dependent interface energy and its applications. *Surf. Sci. Rep.* **2008**, *63*, 427−464.


https://doi.org/10.1021/acsomega.4c09270
*ACS Omega* 2025, 10, 9165−9176

(88) Burke, L. D.; Nugent, P. F. The electrochemistry of gold: I the redox behaviour of the metal in aqueous media. *Gold Bull.* **1997**, *30*, 43−53.
(89) Burke, L. D. Premonolayer oxidation and its role in electrocatalysis. *Electrochim. Acta* **1994**, *39*, 1841−1848.
(90) Larew, L. A.; Johnson, D. C. Concentration dependence of the mechanism of glucose oxidation at gold electrodes in alkaline media. *J. Electroanal. Chem. Interfacial Electrochem.* **1989**, *262* (1−2), 167−182.
(91) Wooten, M.; Shim, J.; Gorski, W. Amperometric Determination of Glucose at Conventional vs. Nanostructured Gold Electrodes in Neutral Solutions. *Electroanalysis* **2010**, *22*, 1275−1277.
(92) Rodríguez-López, J.; Alpuche-Avilés, M. A.; Bard, A. J. Interrogation of Surfaces for the Quantification of Adsorbed Species on Electrodes: Oxygen on Gold and Platinum in Neutral Media. *J. Am. Chem. Soc.* **2008**, *130*, 16985−16995.
(93) Hsiao, M. W.; Adžić, R. R.; Yeager, E. B. Electrochemical Oxidation of Glucose on Single Crystal and Polycrystalline Gold Surfaces in Phosphate Buffer. *J. Electrochem. Soc.* **1996**, *143*, 759−767.
(94) Bard, A. J.; Faulkner, L. R. *Electrochemical methods: fundamentals and applications*, 2nd ed.; Wiley: New York, 2001.
(95) Mocak, J.; Bond, A. M.; Mitchell, S.; Scollary, G. A statistical overview of standard (IUPAC and ACS) and new procedures for determining the limits of detection and quantification: Application to voltammetric and stripping techniques (Technical Report). *Pure Appl. Chem.* **1997**, *69*, 297−328.
(96) Ismail, N. S.; Le, Q. H.; Yoshikawa, H.; Saito, M.; Tamiya, E. Development of Non-enzymatic Electrochemical Glucose Sensor Based on Graphene Oxide Nanoribbon - Gold Nanoparticle Hybrid. *Electrochim. Acta* **2014**, *146*, 98−105.
(97) Shamsabadi, A. S.; Tavanai, H.; Ranjbar, M.; Farnood, A.; Bazarganipour, M. Electrochemical non-enzymatic sensing of glucose by gold nanoparticles incorporated graphene nanofibers. *Mater. Today Commun.* **2020**, *24*, 100963.
(98) Berni, A.; Amine, A.; García-Guzmán, J. J.; Cubillana-Aguilera, L.; Palacios-Santander, J. M. Feather-like Gold Nanostructures Anchored onto 3D Mesoporous Laser-Scribed Graphene: A Highly Sensitive Platform for Enzymeless Glucose Electrochemical Detection in Neutral Media. *Biosensors* **2023**, *13*, 678.
(99) Grochowska, K.; Ryl, J.; Karczewski, J.; Śliwiński, G.; Cenian, A.; Siuzdak, K. Non-enzymatic flexible glucose sensing platform based on nanostructured TiO2 - Au composite. *J. Electroanal. Chem.* **2019**, *837*, 230−239.
(100) Okamoto, K.; Kawakami, H.; Chien, Y.-A.; Kurioka, T.; Chiu, W.-T.; Chakraborty, P.; Nakamoto, T.; Hsu, Y.-J.; Sone, M.; Chang, T.-F. M. Gold/MnO2 particles decorated on electrodeposited polyaniline toward non-enzymatic electrochemical sensor for glucose. *Micro Nano Eng.* **2023**, *18*, 100175.
(101) Makovos, E.; Liu, C. A cyclic-voltammetric study of glucose oxidation on a gold electrode. *Bioelectrochem. Bioenerg.* **1986**, *15*, 157−165.
(102) Pasta, M.; La Mantia, F.; Cui, Y. Mechanism of glucose electrochemical oxidation on gold surface. *Electrochim. Acta* **2010**, *55*, 5561−5568.


https://doi.org/10.1021/acsomega.4c09270
*ACS Omega* 2025, 10, 9165−9176